Available online at www.sciencedirect.com
ScienceDirect
Journal of Power Sources 177 (2008) 355–368
JOURNAL OF POWER SOURCES
www.elsevier.com/locate/jpowsour

Impact of cell design and operating conditions on the performances of SOFC fuelled with methane

J. Laurencin *, F. Lefebvre-Joud, G. Delette

CEA/LITEN/DTH/LEV, 17 avenue des martyrs, 38054 Grenoble, France

Received 20 July 2007; received in revised form 15 November 2007; accepted 24 November 2007
Available online 5 December 2007

Abstract

An in-house-model has been developed to study the thermal and electrochemical behaviour of a planar SOFC fed directly with methane and incorporated in a boiler. The usual Ni-YSZ cermet has been considered for the anode material. It has been found that methane reforming into hydrogen occurs only at the cell inlet in a limited depth within the anode. A sensitivity analysis has allowed establishing that anode thicknesses higher than ~400–500 μm are required to achieve both the optimal methane conversion and electrochemical performances.

The direct internal reforming (DIR) mechanisms and the impact of operating conditions on temperature gradients and SOFC electrical efficiencies have been investigated considering the anode supported cell configuration. It has been shown that the temperature gradient is minimised in the autothermal mode of cell operation. Thermal equilibrium in the stack has been found to be strongly dependent on radiative heat losses with the stack envelope. Electrochemical performance and cell temperature maps have been established as a function of methane flow rates and cell voltages.

Keywords: SOFC; Direct internal reforming; Cermet Ni-YSZ; Modelling

1. Introduction

Solid oxide fuel cells (SOFCs) allow the conversion of chemical energy into electricity. As they operate at high temperatures, they present the advantage of high efficiency and large fuel flexibility. For instance, SOFCs are able to oxidize hydrogen, carbon monoxide, methane and potentially other hydrocarbon fuels (ethanol, methanol, etc.). As the methane represents the main component of the natural gas, it constitutes an interesting fuel for studies. In the most common way, the methane is converted into a mixture of H_2 and CO by using an external reformer. Another way consists in reforming the methane directly within the anode [1,2]. The main advantage of the Direct Internal Reforming (DIR) is to simplify the system since the reformer is suppressed. However, in order to avoid carbon deposition in the electrode, the DIR cell operation requires a large amount of steam in addition to the fuel. Furthermore, the endothermic reforming reaction can induce a local cell cooling and potentially a thermal gradient across the cell. This inhomogeneous temperature along the cell can induce thermal stresses potentially harmful for the cell integrity.

Modelling appears to be an efficient tool to analyse the coupled mechanisms of the DIR process. Indeed, in this operating mode, the molar and heat fluxes within the cell, the rates of both chemical reforming reactions and hydrogen electro-oxidation are coupled together through the temperature field. Several models have been recently developed to describe the DIR process either in tubular [3–8] or planar configurations [9–12]. The description of the multi-component transport within thick anode of a planar cell has been initially proposed by Lehnert et al. [9] in the frame of the mean transport pore model (MTPM). The MTPM model has been then extended by Ackmann et al. [10] into a two-dimensional approach and integrated into models including a thermal analysis [5,12]. In tubular configuration, Sánchez et al. [7] have evaluated the effect of radiative heat exchange on cell performances whereas Klein et al. [8] have studied the gradual internal reforming (GIR). In planar configuration, Aguiar et al. [11] have developed a one-dimensional steady-state and dynamic model taking into account heat transfer by radiation between cells and interconnects. Whereas most of planar configuration models consider only an adiabatic unit cell at the stack centre, Chyou et al. [13] have calculated the

* Corresponding author. Tel.: +33 4 38782210; fax: +33 4 38784139.
E-mail address: laurencin@chartreuse.cea.fr (J. Laurencin).

0378-7753/$ – see front matter © 2007 Elsevier B.V. All rights reserved.
doi:10.1016/j.jpowsour.2007.11.099

heat flux dissipated to the environment by taking into account the stack insulating envelopes. Larrain et al. [14,15] have also developed a model in which the boundary conditions are defined by the radiative heat losses from SOFC edges and by the fuel post combustion.

In this work, an in-house model has been developed to describe the thermo-electrochemical behaviour of a planar stack operating directly with methane. A two-dimensional approach has been adopted to describe the mass transport along the channels and gas diffusion through the anode in the frame of the MTPM model. The kinetics of chemical and electrochemical reactions has been coupled to a thermal analysis. A special attention has been paid on radiative heat losses, usually neglected despite their significant influence. This model has been used to optimize the cell design regarding to the DIR process. Considering the optimal geometry, the mechanisms of the methane reforming and cell operation have been studied. In order to predict the SOFC electrical and thermal management, the effects of the SOFC operating conditions on temperature field and electrochemical performances have been investigated.

2. Model description

2.1. Introduction

A schematic cross-section of the simulated single repeat unit (SRU) is illustrated in Fig. 1. The cell presents a circular shape with a 116 mm diameter. The most common SOFC cell materials have been considered for this study, *i.e.* yttria stabilized zirconia (YSZ) for the electrolyte, Ni-YSZ cermet for the anode and strontium-doped lanthanum manganite (LSM) for the cathode. Interconnect plates have been assumed to be made in Inconel Ni-based alloy. Both the fuel and oxidant are introduced at the cell centre. Fluids channels are designed as part of the metallic interconnect considering a radial flow at the anode and cathode sides (Fig. 2). In order to ensure the current collection, a pattern of small pins has been machined onto the interconnect surface through which oxidant and fuel gases flow. A glass seal is used at the anode side to prevent gas crossover.

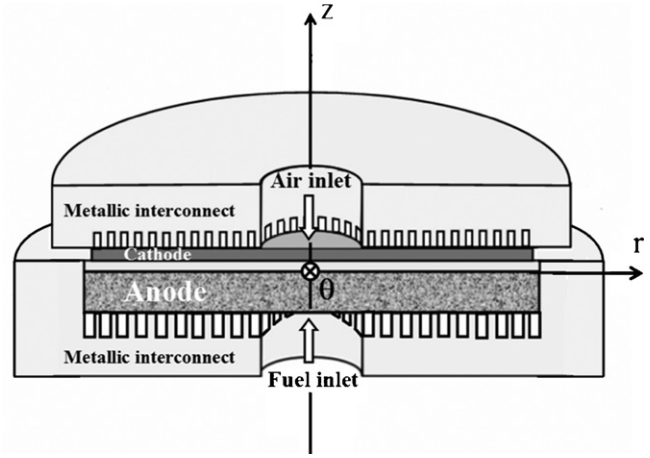

Fig. 1. Scheme of the simulated SRU (cross-section view) and coordinate system used in the model.

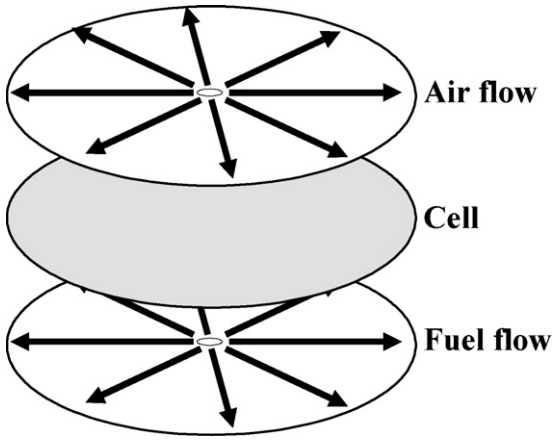

Fig. 2. Configurations for the fuel and air flows [16].

In the present work the fuel considered is a mixture of CH_4 and H_2O with steam to carbon ratio S/C = 1. The conversion of methane into hydrogen is done within the anode through the steam reforming reaction (1). The carbon monoxide, a product of the steam reforming, can be further oxidised through the water gas shift (WGS) reaction (2). The carbon dioxide can also react with methane due to the CO_2 reforming reaction (3):

$$CH_4 + H_2O \leftrightarrow 3H_2 + CO \quad \Delta H^\circ(800\,^\circ C) = +242\,\mathrm{KJ\,mol^{-1}} \tag{1}$$

$$CO + H_2O \leftrightarrow H_2 + CO_2 \quad \Delta H^\circ(800\,^\circ C) = -38.6\,\mathrm{KJ\,mol^{-1}} \tag{2}$$

$$CH_4 + CO_2 \leftrightarrow 2H_2 + 2CO \quad \Delta H^\circ(800\,^\circ C) = +280\,\mathrm{KJ\,mol^{-1}} \tag{3}$$

Hydrogen is finally oxidised according to the following exothermic reaction:

$$H_2 + 1/2O_2 \leftrightarrow H_2O \qquad \Delta H^\circ(800\,^\circ C) = -242\,\mathrm{KJ\,mol^{-1}} \tag{4}$$

In parallel to the methane reforming process, reactions of carbon deposition can also occur. However, these reactions have been neglected in the present work since the S/C ratio of the fuel mixture has been kept constant and equal to 1. Indeed, according to thermodynamic calculations [17], this condition at the considered SOFC operating temperature (*i.e.* 800 °C) prevents any carbon deposition.

The coordinate system used for the modelling is shown in Fig. 1. Because of the circular geometry of the SRU, a two-dimensional approach has been adopted assuming z as an axisymmetrical axis. The model has been basically divided into two connected modules: the electrochemical one and the thermal one. The electrochemical part of the model has been implemented in the software tool Matlab. It allows determining the local current density, the distribution of gas species and the

thermal sources related to the chemical and electrochemical reactions. The thermal module has been implemented in a finite element solver, Cast3M [18]. It allows determining the thermal fluxes and temperature field in both the solid and gas phases of the SRU. The two modules have been coupled through:

(i) the temperature field required to determine the kinetic constants of chemical and electro-chemical reactions,
(ii) the heat source terms necessary to simulate the temperature field,
(iii) the gas composition modified along the channels necessary to calculate the fluids thermal properties.

2.2. Description of the electrochemical module

A detailed description of the electrochemical module is given elsewhere [12]. Evolution of molar fractions along the gas channels (*i.e.* in the radial direction r) is caused by normal molar fluxes (*i.e.* in the axial direction z) through the porous electrodes. This evolution is calculated with mass balance performed on each species along the gas channels.

The mass transport through the porous anode (*i.e.* in the axial direction z) has been described in terms of the Stephan-Maxwell and Knudsen diffusion. The diffusion coefficients have been calculated according to Todd and Young [19] as a function of the microstructure parameters (mean pore radius $\langle r \rangle$, tortuosity τ and porosity ε). It has been assumed that the steam and carbon dioxide reforming reactions occur within the anode on the pore surfaces whereas the water gas shift takes place in the void fraction of the anode (Fig. 3). The kinetic constants for both steam and CO_2 reforming reactions ((1) and (3)) have been considered for Ni catalyst and taken from references [12,20]. Furthermore, only hydrogen electro-oxidation is taken into account. This assumption means that a large fraction of CO is converted into CO_2 through the water gas shift reaction (2), which is supposed to be fast and always close to the thermodynamic equilibrium. The hydrogen electro-oxidation (4) is assumed to occur at the anode/electrolyte interface (Fig. 3). The corresponding molar flux density $\dot{N}_{H_2}$ is related to the local current density i by the

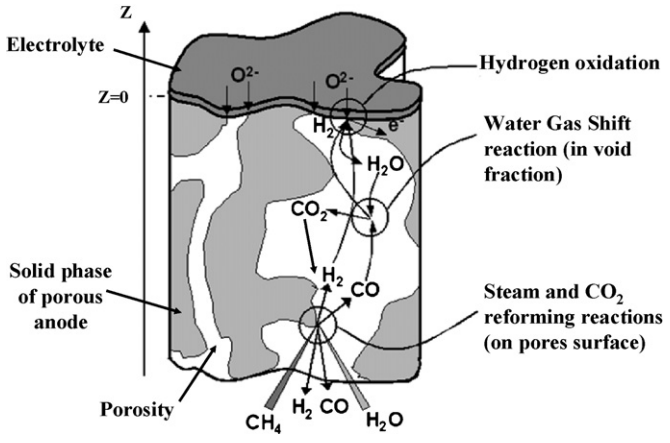

Fig. 3. Localisation within the anode of the reforming reactions. The H_2 oxidation is assumed to take place at the anode/electrolyte interface.

Faraday's law:

$$\dot{N}_{H_2} = \frac{i}{2F} \tag{5}$$

where F is the Faraday's constant.

The cell voltage U_{cell} is fixed and assumed to be constant on the whole cell area. The local current density is calculated in order to verify the following equation all along the cell:

$$U_{cell} = E_{i=0} - (R_{ohm})i - (\eta_{conc,a} + \eta_{conc,c} + \eta_{act}) = f(i) \tag{6}$$

where $E_{i=0}$ is the open circuit voltage (OCV) and η_{conc} the concentration overpotentials (the subscripts a and c represent the anode and cathode, respectively). The term R_{ohm} corresponds to the pure ohmic cell resistances including the electrolyte ionic resistance R_e and the contact resistance R_c between interconnects and electrodes. The term η_{act} represents the activation overpotential calculated from the Butler-Volmer equation:

$$\eta_{act} = \frac{RT}{F} \operatorname{arcsin} h \left(\frac{i}{2i_0} \right) \tag{7}$$

where i_0 is the exchange current density for the cell, R the gas constant and T is the temperature. The OCV and the anodic concentration polarisation have been written according to the Nernst's equation:

$$E_{i=0} = E_0(T) + \frac{RT}{2F} \ln \frac{P_{H_2}^{TPB_a,i=0} (P_{O_2}^{TPB_c,i=0})^{0.5}}{P_{H_2O}^{TPB_a,i=0}} \tag{8a}$$

$$\eta_{conc,a} = \frac{RT}{2F} \ln \frac{P_{H_2O}^{TPB_a,i\neq 0} P_{H_2}^{TPB_a,i=0}}{P_{H_2}^{TPB_a,i\neq 0} P_{H_2O}^{TPB_a,i=0}} \tag{8b}$$

where E_0 is the standard potential and P_j the partial pressures at OCV ($i = 0$) or under current ($i \neq 0$). The superscripts TPB_a and TPB_c denote the triple phase boundaries at anode and cathode sides which have been reduced in the model at the anode/electrolyte and cathode/electrolyte interfaces, respectively. It is worth noting that this assumption is well verified for sufficiently thick electrodes. Indeed, Kim et al. [21] have shown that the reaction zone spreads only about 10 μm from the electrolyte/electrode into the electrode.

The cathodic concentration overpotential $\eta_{conc,c}$ has been described by a phenomenological law depending on the limiting current density $i_{lim,c}$. A high value has been taken for this last parameter since a high air ratio and a thin cathode have been considered for the simulations (see Section 3). The microstructural and electrochemical parameters used for the present work are listed in Table 1.

2.3. Description of the thermal module

2.3.1. Boundary conditions

Adiabatic conditions have been assumed for the surfaces connecting two adjacent SRUs (*i.e.* the bottom and top free surfaces of SRU as shown in Fig. 4). This assumption is rigorously right only for the SRUs placed in the central region of the stack where

Table 1
Microstructural and electrochemical parameters of the model used for the simulations

Electrochemical parameters		
R_c	Contact resistances between electrode/interconnects (ohm cm^2)	0.2
i_0	Cell exchange current density (mA cm^{-2})	100 [21]
$i_{lim,c}$	Cathodic limiting current density (mA cm^{-2})	1000
σ_i	Ionic conductivity of electrolyte (YSZ) (ohm^{-1} cm^{-1})	0.035 (T = 800 °C) [22]
Microstructural parameters		
ε	Electrode porosity	0.4
τ	Electrode tortuosity	4
$\langle r \rangle$	Electrode mean pore radius (μm)	1

heat flux in the stacking direction can be neglected. Gases introduced at cell centre are assumed to have a controlled temperature equal to 800 °C. The temperature of the insulating envelope surrounding the stack is also supposed to be maintained to 800 °C. This last assumption is representative of a stack tested in a furnace or placed directly into a boiler.

2.3.2. Energy balance for fluids along the gas channels (in the radial direction)

The fuel and air gas properties are modified along the channels between interconnect and electrodes as their compositions are changing. These modifications are taken into account in the thermal part of the model. Indeed, according to the radial position r in the gas channels, the isobaric heat capacity C_p, the thermal conductivity λ, and the dynamic viscosity η are calculated for each species. The polynomial curves established by Todd and Young [19] have been used to calculate these properties for fuel and air gases.

The determination of the Reynolds number Re has shown that, in the studied conditions, a laminar flow takes place inside the fuel and air channels. According to the results of Damn et al. [23] and Sánchez et al. [7], the radiative heat exchange between gases and walls can be neglected. Finally, the energy balances for air and fuel channels confined between the electrodes and interconnect plates have been written as follows:

$$\sum_i \dot{n}_i(r) C_p^i(r) \frac{\partial T_{fuel}}{\partial r} dr = h_{fuel}(r) dS \{T_s(r) - T_{fuel}(r)\}$$
$$(i = H_2, H_2O, CO, CO_2, CH_4) \quad (9a)$$

$$\sum_i \dot{n}_i(r) C_p^i(r) \frac{\partial T_{air}}{\partial r} dr = h_{air}(r) dS \{T_s(r) - T_{air}(r)\}$$
$$(i = O_2, N_2) \quad (9b)$$

where $\dot{n}_i$ represents the molar flow rate and C_p^i the heat capacity for each gas species i. The terms T_{air} and T_{fuel} correspond to the temperature of oxidant and fuel, respectively, whereas T_s denotes the wall temperature of solid phase. The exchange surface dS corresponds to the contact area between gas and solid and takes into account the surface added by the small pins of the interconnect plate. The convective heat transfer coefficients $h_{air/fuel}$ has been computed from the Nusselt number Nu as follows:

$$h_{air/fuel} = \frac{Nu \lambda_{air/fuel}}{D_H} \quad (10)$$

where D_H is the hydraulic diameter of the cathodic or anodic channel. The Nusselt number tends to an asymptotic value, provided that a fully developed laminar flow is achieved in the channels. In this work, the Nusselt number has been taken to 5.38, value corresponding to a flow confined between two plates (with one side adiabatic) [13].

As illustrated in Fig. 5a, the heat transfer coefficient h_{fuel} for fuel is observed to be strongly affected by its radial position in the anodic channel. Indeed, the DIR process transforms the steam and methane into a mixture rich in hydrogen which is then oxidised. As this last component presents a much higher thermal conductivity than other fuel species, the heat transfer coefficient is strongly dependant of the amount of hydrogen produced and consumed along the anodic channel. In addition, the

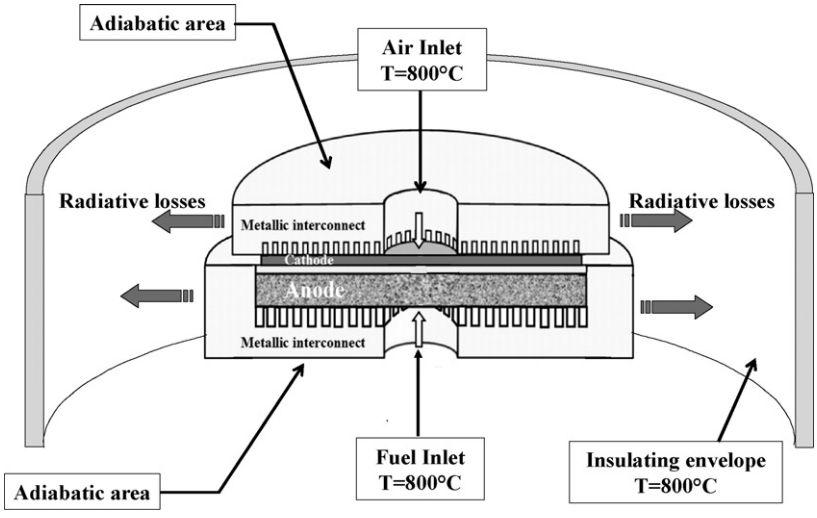

Fig. 4. Boundary conditions assumed for the thermal simulations.

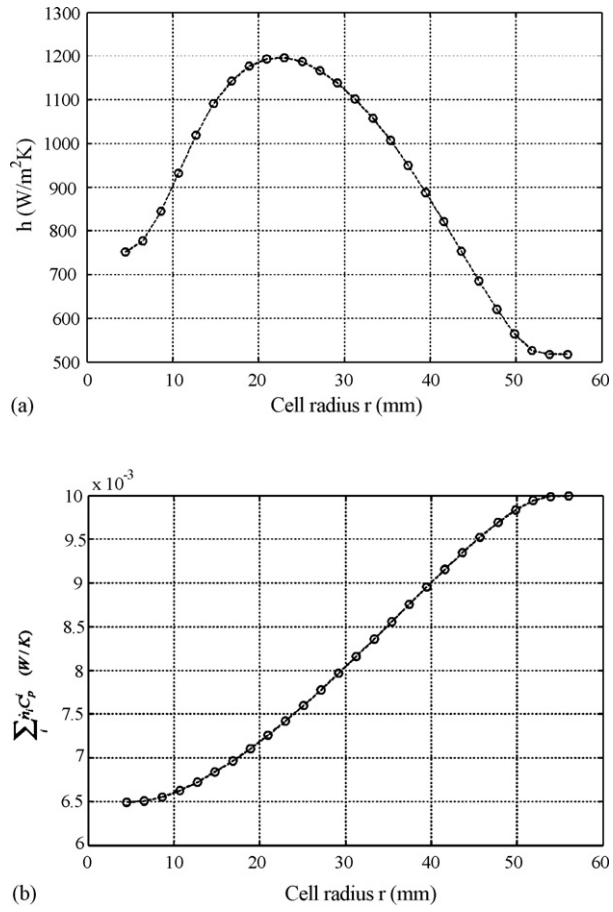

Fig. 5. Evolution of the fuel heat transfer coefficient and $\sum_i \dot{n}_i C_p^i$ term plotted as a function of the radial position in the cell (for $\dot{n}_{CH_4} = 5.507 \times 10^{-5}$ mol s^{-1}, $\dot{n}_{H_2O}/\dot{n}_{CH_4} = 1$ and $U_{cell} = 600$ mV). (a) Fuel heat transfer coefficient and (b) $\sum_i \dot{n}_i C_p^i$ term of fuel.

$\sum_i \dot{n}_i C_p^i$ terms are also modified because of the chemical and electrochemical reactions (Fig. 5b). Therefore, the evolutions of h and $\sum_i \dot{n}_i C_p^i$ terms due to the variation of the fluids composition along the channels have been taken into account in the DIR modelling.

2.3.3. Energy balance for fluids in the inlet compartments

Energy balances equivalent to Eqs. (9a) and (9b) have been also written for the fuel and oxidant inlet compartments. The heat transfer coefficients have been calculated at the anode and cathode side by using Eq. (10), assuming an asymptotic Nusselt number equal to 3.6 [7,13]. Such energy balances allow determining the gas temperatures at the inlet of the air and fuel flow channels (confined between electrodes and interconnect plates).

2.3.4. Energy balance for the solid phases of the SRU

The governing equation to calculate the temperature of the solid phase has been expressed considering conduction, convection and radiation. For a solid volume, dV, in contact with the fluid on a surface, dS, the energy balance has been written as follows:

$$\lambda \nabla^2 T_s \, dV + d\dot{Q} = h_{fluid} dS \{T_s - T_{fluid}\} + d\dot{\phi}_{rad} \quad (11)$$

The first term of this equation, $\lambda \nabla^2 T_s \, dV$, is related to the heat transport by conduction in the solid phases. The term λ represents the thermal conductivity of the solid volume dV. It is worth noting that the porous anode and cathode have been modelled as homogenous media in which only conduction is taken into account. Indeed, the Peclet number Pe calculated within the electrodes remains much lower than unity, meaning that the heat transport by convection is negligible in comparison to conduction [10]. The effective thermal conductivity of the porous electrodes can then be determined considering a mixture law between the conductivities of solid and fluid regions [8].

The second term of Eq. (11), d$\dot{Q}$, corresponds to the thermal sources related to the electrochemical and chemical reactions:

- The first contribution to d$\dot{Q}$ is the heat generation, d$\dot{q}_{ox}$, due to the hydrogen oxidation:

$$d\dot{q}_{ox} = \left\{ \frac{i(r)}{2F} \Delta H_{H_2O} + i(r) U_{cell} \right\} dS \quad (12)$$

Considering Eqs. (6) and (12) can also be expressed as follows:

$$d\dot{q}_{ox} = \left[\frac{i(r)}{2F} \Delta H_{H_2O} + E_{i=0} i(r) - R_e i^2(r) - R_c i^2(r) - (\eta_{conc,a} + \eta_{conc,c} + \eta_{act}) i^2(r) \right] dS \quad (13)$$

The heat linked to the SRU contact resistances, $-R_c i^2$, has been supposed to be released at the electrode/interconnect interfaces. The heat due to the electrolyte resistance, $-R_e i^2$, has been located in the volume of the electrolyte layer. The other heat sources (*i.e.* $(i/2F)\Delta H_{H_2O} + E_{i=0} i - (\eta_{conc,a} + \eta_{conc,c} + \eta_{act}) i^2$) are likely released at the electrode/electrolyte interfaces. However, since the anode and cathode contributions are difficult to separate, these heat sources have been delocalised in the electrolyte layer.

- The second contribution to d$\dot{Q}$ corresponds to the heat generation, d$\dot{q}_{ref}$, due to the reforming chemical reactions ((1)–(3)). Corresponding heat source terms have been located within the porous anode and are expressed as a function of the reaction rates v_i:

$$d\dot{q}_{ref} = \left\{ \sum_{i=1}^{i=3} v_i(r, z) \Delta H_i \right\} dV \quad (14)$$

The last term of Eq. (11), d$\dot{\phi}_{rad}$, is related to the heat transfer by radiation and has been divided into two contributions:

- The first one, d$\dot{\phi}_1$, corresponds to the solid surface-to-surface heat exchange between electrodes (anode or cathode) and interconnects plates. It has been approximated in the model according to the general expression between two infinite parallel planes

$$d\dot{\phi}_1 = \left\{ \frac{\sigma \varepsilon_{anode/cathode} \varepsilon_{interconnect}}{1-(1-\varepsilon_{anode/cathode})(1-\varepsilon_{interconnect})} (T^4_{anode/cathode} - T^4_{interconnect}) \right\} dS \quad (15)$$

Table 2
Material thermal parameters at SOFC operating temperature

	Anode	Electrolyte	Cathode	Interconnect
Conductivity λ ($W\,m^{-1}\,K^{-1}$)	6 [8]	3.8 [24]	11 [8]	25 [15]
Emissivity ε	0.4 [8]	–	0.4 [8]	0.7

where ε denotes the emissivity of materials (for anode, cathode and interconnects) and σ the Stefan-Boltzmann's constant.

- The second contribution to $d\dot{\phi}_{rad}$ corresponds to the radiative heat losses, $d\dot{\phi}_2$, flowing from the SRU to the stack insulating envelope:

$$d\dot{\phi}_2 = \{\sigma\varepsilon_{interconnect}(T_s^4 - T_{insulating}^4)\}dS \quad (16)$$

where T_s denotes the surface temperature taken on the free edge of the SRU. The term $T_{insulating}$ corresponds to the stack envelope temperature taken here at 800 °C (Fig. 4). The thermal parameters for materials considered in the model are provided in Table 2. According to Larrain et al. [14], the interconnect emissivity, $\varepsilon_{interconnect}$, depends on the metal surface state and can vary over a large range from 0.4 to 0.9. For the present simulations, this parameter has been fixed to the value equal to ~0.7. Indeed, a sensitivity analysis carried out for the present study has shown that the modification of this last parameter between 0.6 and 0.8 has no major influence on the final temperature field.

3. Results and analysis

3.1. Influence of anode thickness on cell performances

Cathode and electrolyte thicknesses have been fixed to 60 μm and 150 μm, respectively. Electrochemical performances have been investigated as a function of the anode thickness within the range 60–2200 μm. Simulations have been performed with a 98.5 cm^2 active cell area. The polarisation curves have been simulated with an inlet methane flow rate of $\dot{n}_{CH_4} = 14.686 \times 10^{-5}$ mol s^{-1} and an air ratio $\Re_{air} = \dot{n}_{air}/\dot{n}_{fuel}$ equal to 3. The results are given in Fig. 6 and show that the electrochemical performances are strongly improved by increasing the anode thickness up to around 1000 μm. Beyond this last value, the polarisation curves are almost similar. It is worth noting that both the OCV and cell limiting current are simultaneously increased with the anode thickness.

As shown in Fig. 7, the methane conversion into hydrogen is found to be increased with the anode thickness. It is consistent with the fact that a sufficient number of catalytic sites is required for the steam and CO_2 reforming reactions to occur. As a consequence, the hydrogen production is found to be limited when the anode layer is too thin.

The electrochemical performance improvements obtained by increasing the anode thickness can thus be linked to the amount of hydrogen produced at the anode side by the reforming reactions. Indeed, the high quantities of hydrogen in the fuel mixture obtained with thicker anodes as shown in Fig. 7 explained the high OCV values (Fig. 8). The cell limiting current linked to

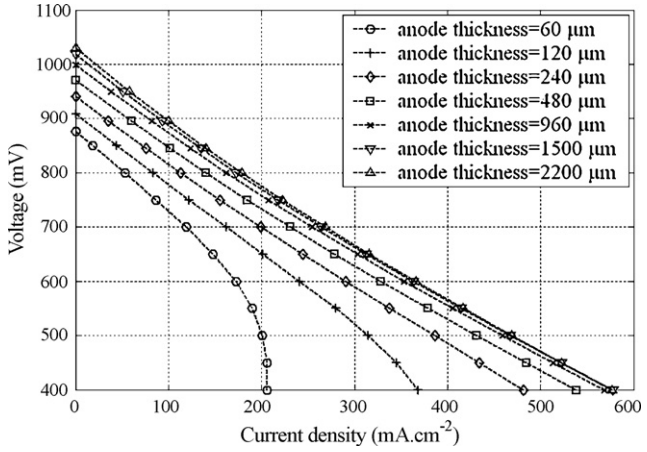

Fig. 6. Polarisation curves plotted for different anode thicknesses ($\dot{n}_{CH_4} = 14.686 \times 10^{-5}$ mol/s, $\dot{n}_{H_2O}/\dot{n}_{CH_4} = 1$, $\Re_{air} = 3$, active cell area = 98.5 cm^2).

anodic concentration overpotential $\eta_{conc,a}$ increases with anode thickness. The term $\eta_{conc,a}$ has been plotted in Fig. 9 as a function of the anode thickness (for $U_{cell} = 500$ mV). For the thinnest layers (<500 μm), the high concentration overpotentials are related to a hydrogen starvation at the anode/electrolyte interface caused by a too low hydrogen production rate within the bulk cermet. Inversely, for thick anodes (>500 μm), concentration overpotentials slowly increase because of mass transfer limitations: the hydrogen transport to the anode/electrolyte interface is hindered by diffusion of species through the porous thick electrode.

It can be noticed in Fig. 7 that the methane conversion rate tends to an asymptotic value for the highest anode thicknesses (around 80% for the present condition of fuel supply). This result suggests that the depth of the methane reaction zone in

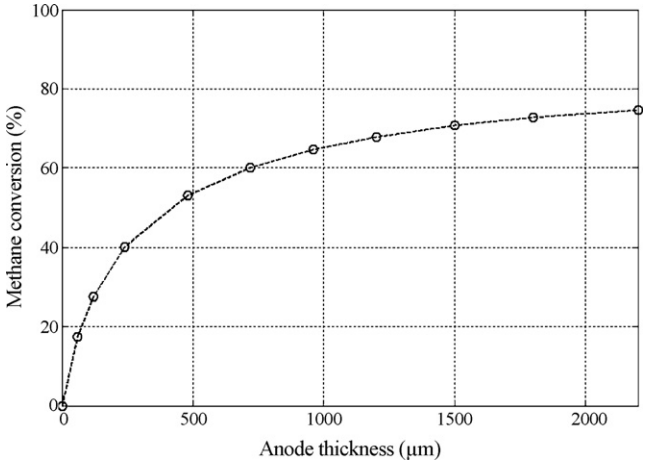

Fig. 7. Methane conversion plotted as a function of the anode thickness at the OCV ($\dot{n}_{CH_4} = 14.686 \times 10^{-5}$ mol/s, $\dot{n}_{H_2O}/\dot{n}_{CH_4} = 1$, $\Re_{air} = 3$).

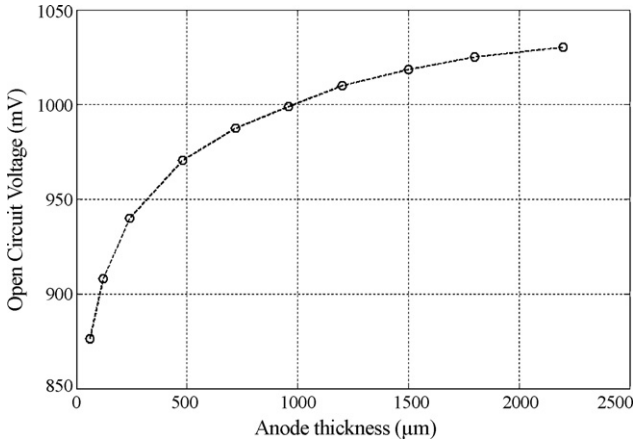

Fig. 8. OCV plotted as a function of the anode thickness ($\dot{n}_{CH_4} = 14.686 \times 10^{-5}$ mol/s, $\dot{n}_{H_2O}/\dot{n}_{CH_4} = 1$, $\Re_{air} = 3$).

the porous electrode is limited. In order to illustrate this last remark, the reforming reactions rates (Fig. 10a) and the resulting hydrogen production rate (Fig. 10b) have been plotted as a function of their axial locations (z) across the anode at cell centre ($r = 0$) and at OCV. The curves of Fig. 10a and b refer to a 2200 μm anode thickness. The hydrogen production rate is found to be directly controlled by the steam reforming reaction rate which is significantly higher than the rates of the other reactions. As the steam-reforming rate decreases strongly from the anode entrance surface layer up to the anode/electrolyte interface, the hydrogen production rate drops similarly inside the

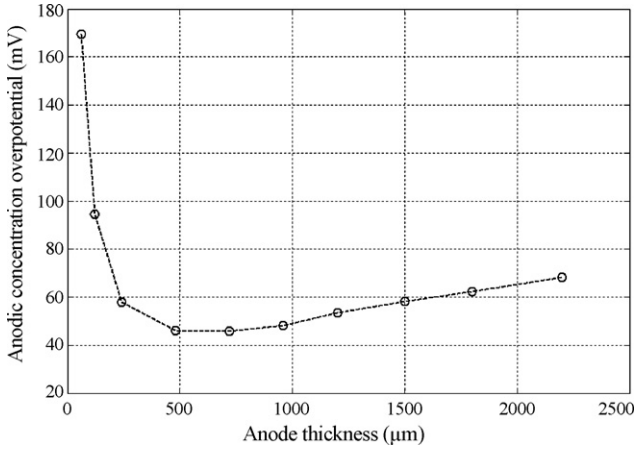

Fig. 9. Anodic concentration overpotential plotted as a function of the anode thickness at a cell voltage $U_{cell} = 500$ mV ($\dot{n}_{CH_4} = 14.686 \times 10^{-5}$ mol/s, $\dot{n}_{H_2O}/\dot{n}_{CH_4} = 1$, $\Re_{air} = 3$).

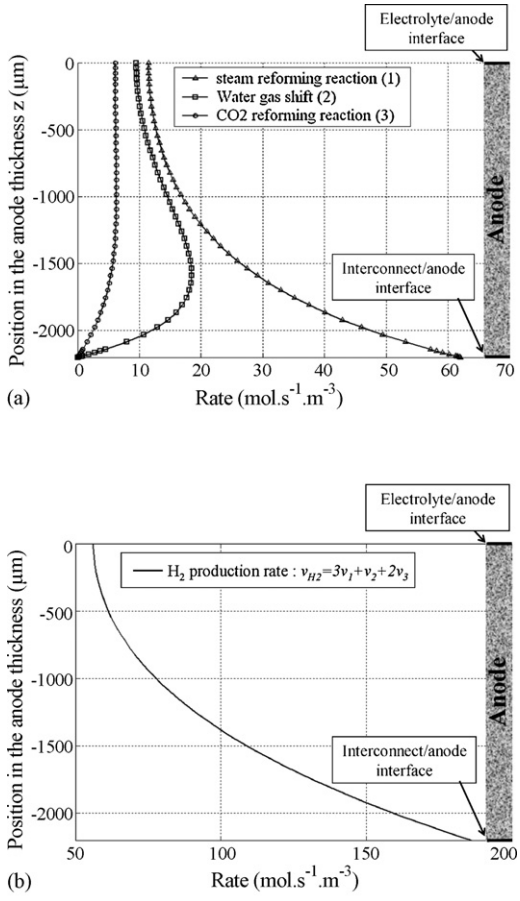

Fig. 10. Reaction rates plotted as a function of their axial position z within the anode at the cell centre $r = 0$ and for the OCV (anode thickness = 2200 μm, $\dot{n}_{CH_4} = 14.686 \times 10^{-5}$ mol/s, $\dot{n}_{H_2O}/\dot{n}_{CH_4} = 1$, $\Re_{air} = 3$). (a) Reforming reactions rates, (b) Hydrogen production rate (v_1, v_2 and v_3 refer to reactions (1), (2) and (3)).

anode material (Fig. 10b). Consequently, although an increase of the anode layer thickness improves the total hydrogen production, this improvement becomes less and less pronounced and leads to the observed saturation behaviour.

The evolution of the chemical reaction rates along the axial position (z) in the anode is explained by the repartition of gas species within the cermet. As shown in Fig. 11, the methane and water molar fractions decrease from the entrance surface of the anode to the electrolyte interface. Indeed, these species are readily consumed by the steam reforming reaction resulting in a decrease in the steam reforming reaction rate as observed in Fig. 10a. It is worth noting that the mass transfer limitation by diffusion impedes the molar fraction homogenisation

Table 3
Simulated inlet fuel and air molar flow rates

Conditions of gas feeding	$\dot{n}^{Inlet}_{CH_4}(\times 10^{-5}\,mol\,s^{-1})$	$\dot{n}^{Inlet}_{H_2O}(\times 10^{-5}\,mol\,s^{-1})$	$R = \dot{n}^{inlet}_{H_2O}/\dot{n}^{inlet}_{CH_4}$	$\dot{n}^{inlet}_{air}(\times 10^{-5}\,mol\,s^{-1})$[a]	$\Re_{air} = \dot{n}^{inlet}_{air}/\dot{n}^{inlet}_{fuel}$
I	14.686	14.686	1	88.116	3
II	11.015	11.015	1	88.116	4
III	7.343	7.343	1	88.116	6
IV	5.507	5.507	1	88.116	8

[a] $\dot{n}^{inlet}_{air} = \dot{n}^{inlet}_{O_2} + \dot{n}^{inlet}_{N_2}$ ($\dot{n}^{inlet}_{O_2} = 18.504 \times 10^{-5}\,mol\,s^{-1}$ and $\dot{n}^{inlet}_{N_2} = 69.612 \times 10^{-5}\,mol\,s^{-1}$).

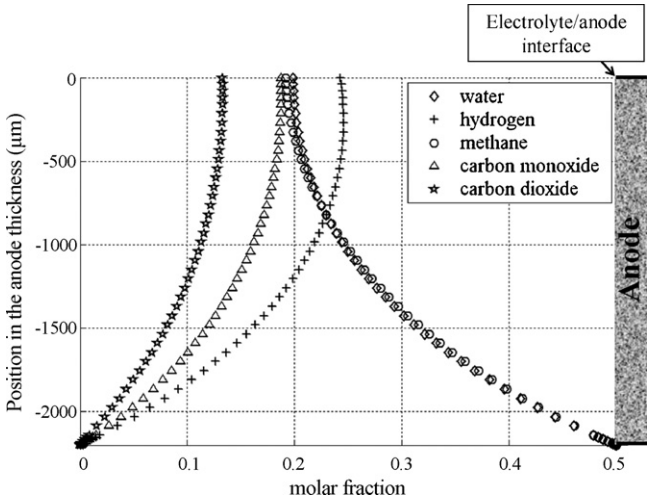

Fig. 11. Molar fraction of fuel species plotted as a function of the anode thickness at the OCV (anode thickness = 2200 µm, $\dot{n}_{CH_4} = 14.686 \times 10^{-5}$ mol/s, $\dot{n}_{H_2O}/\dot{n}_{CH_4} = 1$, $\Re_{air} = 3$).

through the porous anode. This dependence of methane concentration with the position in the anode depth is in good agreement with the simulation results established by Lehnert et al. [9].

As illustrated in Fig. 10a, the CO_2 reforming reaction rate is observed to slightly increase across the anode. This trend is explained by the carbon dioxide production due to the water gas shift reaction which is always shifted towards more H_2 and CO_2 species (Fig. 10a). This effect is activated in the anode entrance layers (near the fuel channel) because of the high amount of H_2O in the fuel and the CO production by the steam reforming reaction (Fig. 11). However, it is limited in the region close to the anode/electrolyte interface because of the high amount of hydrogen and the decrease of water molar fraction.

It can be concluded from this section that the achievement of efficient methane conversion rate into hydrogen requires a minimum anode thickness. However, above a certain value, the CH_4 conversion rate reaches an asymptotic value which is explained by the limitation of the reforming reaction rates due to the dilution of the reactants with the products. This can be attributed to an insufficient diffusion of the species into the porous anode that hinders any homogenisation.

3.2. SRU operation fuelled directly with methane

The mechanisms involved in the DIR process have been investigated under cell polarisation. Taking advantage of the previous analysis, an anode supported cell has been considered with the anode, electrolyte and cathode thicknesses fixed, respectively to 1000, 20 and 60 µm. The active cell area has been taken equal to 98.5 cm^2. The inlet molar fuel flow rate and cell polarisation have been varied to study the SRU operation. Table 3 summarises the investigated cell gas feeding conditions. It can be noticed that the air-flow rate has been kept constant to $\dot{n}_{air}^{inlet} = 88.116 \times 10^{-5}$ mol s^{-1}.

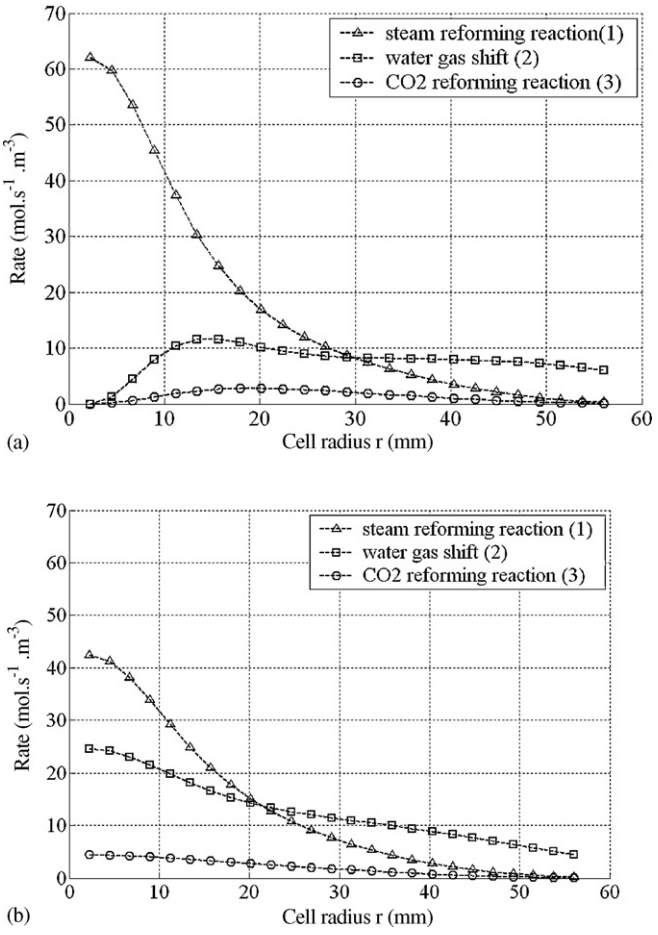

Fig. 12. Evolution of the reforming reaction rates along the cell from the gas inlet (cell centre $r = 0$) to the gas outlet (cell edge $r = r_{max}$) ($U_{cell} = 600$ mV, condition III of cell gas feeding, fuel utilisation = 91.5%). (a) Close to the interconnect/anode interface (at the anode side) and (b) Close to the electrolyte/anode interface (at the anode side).

3.2.1. Mechanisms involved in the DIR process: evolution of molar fractions, temperatures and overpotentials along the cell

The variations of the output parameters of the model along the cell radius are presented for a selected condition of SRU gas feeding (condition III of Table 3). The cell polarisation has been fixed to 600 mV. Fig. 12a and b present the rate of the reforming and WGS reactions within the cermet close to the interfaces with interconnect and electrolyte. As already discussed in the previous section, the steam reforming reaction rate is higher in the entrance layer of the cermet than in the neighbourhood of the anode/electrolyte interface. The same behaviour is observed along the cell radius: the reaction is strongly enhanced at the cell inlet and decreases up to the cell outlet. It can be concluded from these results that, in the DIR process, the effective zone participating to the methane conversion is confined in a limited volume at the anode inlet.

Fig. 13a and b present the evolutions of the molar fraction along the cell from the gas inlet (cell centre $r = 0$) to the gas outlet (cell edge $r = r_{max}$). The CH_4 molar fraction is found to decrease along the cell radius since it is consumed by the reforming process. Hydrogen concentration increases at the cell inlet

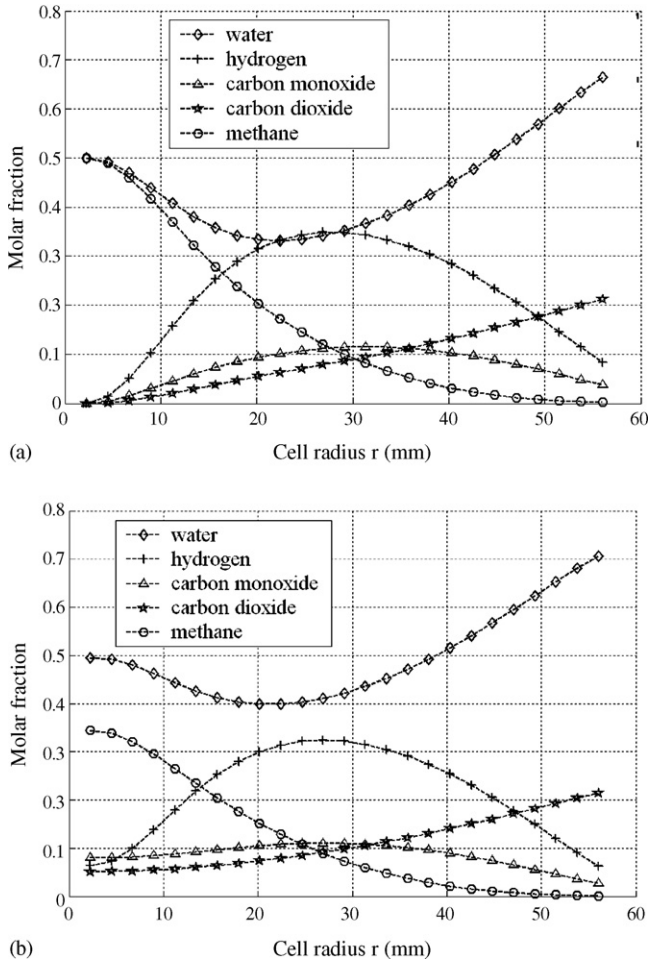

Fig. 13. Evolution of the molar fraction along the cell from the gas inlet (cell centre $r = 0$) to the gas outlet (cell edge $r = r_{max}$) ($U_{cell} = 600$ mV, condition III of cell gas feeding, fuel utilisation = 91.5%). (a) At the interconnect/anode on the anode side and (b) At the electrolyte/anode on the anode side.

because the methane conversion mainly occurs in this region. After a maximum, the hydrogen molar fraction decreases progressively until the cell outlet as it is oxidised all along the cell radius. The same evolution is observed for the carbon monoxide. Indeed, CO is also produced at the cell inlet by the steam reforming reaction and then converted into hydrogen and carbon dioxide through the water gas shift reaction. The water molar fraction follows an inverse evolution than H_2 and CO. Indeed, after a decrease caused by its consumption by the steam reforming reaction, H_2O concentration is observed to increase due to the hydrogen oxidation reaction. It is worth noting that Aguiar et al. [11] have found similar profiles of molar fractions along the cell length for a SOFC operated directly with methane.

Fig. 14 presents the evolution of the overpotentials along the cell radius. It can be verified that the sum of the overpotentials is equal to the difference between the OCV and the cell voltage. This result means that Eq. (6) is well verified and demonstrates the correct convergence of simulations. According to Eq. (8b), the evolution of the anodic concentration overpotential along the cell radius is governed by the values taken by the $P_{H_2O}^{TPB_a, i\neq 0} / P_{H_2}^{TPB_a, i\neq 0}$ ratio.

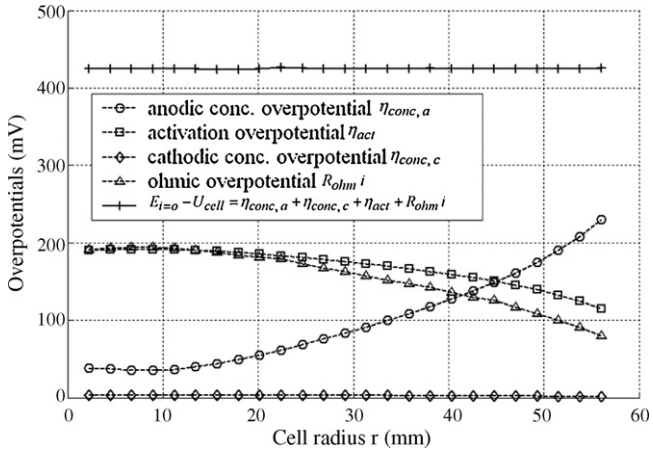

Fig. 14. Evolution of the overpotentials along the cell radius ($U_{cell} = 600$ mV, OCV = 1025 mV, condition III of cell gas feeding, fuel utilisation = 91.5%).

Temperature profiles along the cell radius have been plotted in Fig. 15 at the anode/electrolyte interface and for the interconnect plates. It is verified that temperatures are increased from the cell inlet in the radial direction corresponding to the air and fuel co-flow. In the present case of simulation ($U_{cell} = 600$ mV), the endothermic heat absorbed by the reforming process is lower than the exothermic one released by the hydrogen oxidation. In such conditions, the net resulting heat has to be exhausted from the SRU: the temperature elevation is then due to the heat accumulation stored in the moving fluids. This phenomenon leads to a steep thermal gradient at the cell inlet which is strengthened by the cooling effect due to the endothermic reforming reactions. Indeed, the reforming process occurs essentially at the cell entrance whereas the exothermic hydrogen oxidation takes place all along the cell length. For this reason, the cell exhibits a lower temperature at the cell centre than the interconnect plates. However, the temperature gradient across the SRU (in the z axial direction) is slight because of the adiabatic conditions considered for the modelling.

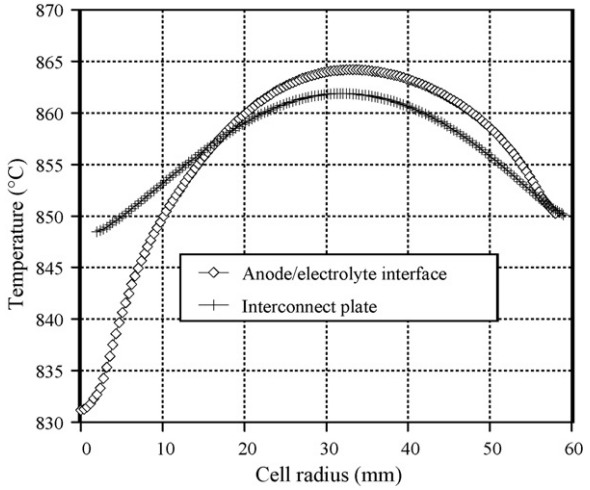

Fig. 15. Temperature evolution plotted along the cell radius for the anode/electrolyte interface and for the interconnect plate ($U_{cell} = 600$ mV, condition III of cell gas feeding, fuel utilisation = 91.5%, temperature of the interconnect plate taken on the surface connecting two adjacent SRUs).

It can be observed that temperatures reach maximum values before the cell outlet. This cooling effect near the SRU periphery can be explained by radiative heat losses with the stack-insulating envelope. For the present conditions of simulation, the maximum temperature is around 865 °C leading to a maximum thermal gradient of around ~3 °C mm^{-1}. This cell warming is relatively lower than the one predicted by Aguiar et al. [11] (considering equivalent fuel utilisation and gas inlet temperature). Indeed, in their case, the heat generated by the electrochemical and chemical reactions could only be exhausted by the air and fuel flows. In the present results, it is shown that the main part of the generated heat is exhausted by radiative heat transfers with the insulating envelope: only ~10% of the heat sources are removed from SRU by the air and fuel streams whereas the ~90% remaining heat are dissipated by radiation towards the insulating envelope.

3.2.2. *Influence of the operating conditions on temperatures and cell performances*

In order to predict the SRU operation when incorporated in the boiler and fed directly with methane, simulations have been performed by varying the cell polarisation and the fuel flow rate introduced at the anode inlet (see flow conditions given in Table 3). Obtained power densities are plotted in Fig. 16. The fuel utilisation U_f has been calculated by using Eq. (17) and is given in Fig. 17:

$$U_f = \frac{I}{8F\dot{n}_{CH_4}^{inlet}} \quad (17)$$

with I is the total current across the cell, F the Faraday's constant and $\dot{n}_{CH_4}^{inlet}$ is the inlet methane molar flow rate.

In Fig. 16, it can be seen that the power density increases logically with the inlet methane flow rate and the cell polarisation. On the other hand, the fuel utilisation is raised when the cell voltage and the methane flow rate are lowered (Fig. 17). For the standard 0.7 Volts operating cell voltage, the fuel utilisation ranges from ~81% for the lowest investigated methane flow rate down to ~38% for the highest one. These conditions correspond respectively to a power density varying from ~250 mW cm^{-2} to ~280 mW cm^{-2}.

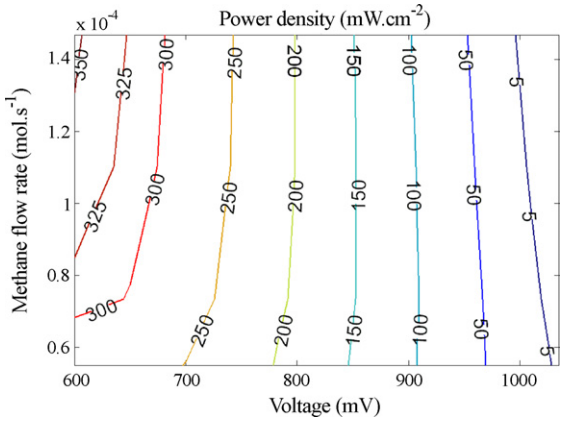

Fig. 16. Maps of power densities plotted as a function of inlet methane flow rate and cell voltage.

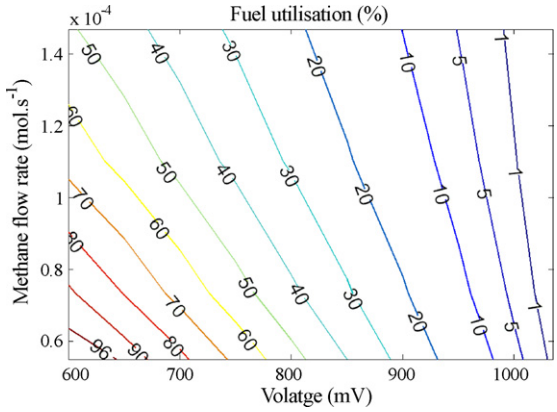

Fig. 17. Maps of fuel utilisations plotted as a function of inlet methane flow rate and cell voltage.

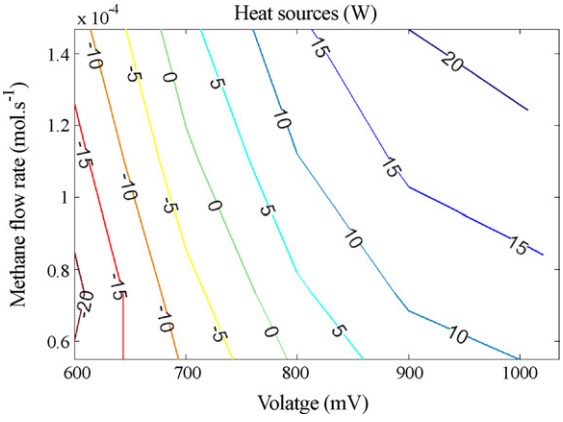

Fig. 18. Map of heat sources plotted as a function of inlet methane flow rate and cell voltage.

Fig. 18 presents the sum of heat sources generated within the cell, corresponding to the endothermic contribution of the reforming process Eq. (14) and to the exothermic contribution of the hydrogen oxidation Eq. (12). The associated maximum temperatures reached in the cell are provided in Fig. 19. The autothermal conditions of cell operation correspond in Fig. 18 to the border line between exothermic and endothermic domain, where heat sources are equal to 0 Watts. These conditions lead in

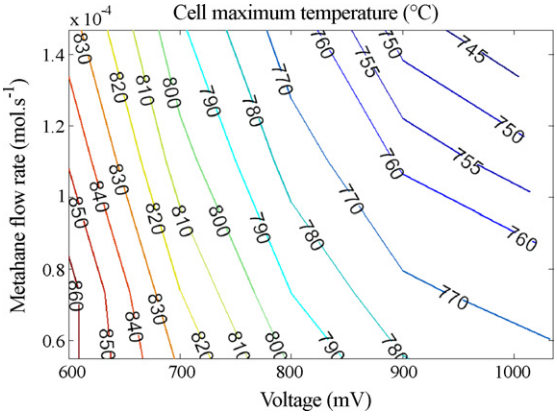

Fig. 19. Map of cell temperatures plotted as a function of inlet methane flow rate and cell voltage.

Fig. 19 to a cell temperature equal to around 800 °C which corresponds to the model boundary temperature taken for the gas inlet and insulating envelope. Exothermic conditions are achieved for the highest cell polarisations and the lowest methane flow rates. In this case, endothermic thermal fluxes due to the reforming process are lower than the absolute value of exothermic thermal fluxes. As observed in Fig. 19, exothermic conditions lead to cell temperatures exceeding the inlet gas temperature. At the opposite side, close to the OCV, exothermic fluxes fall to zero and the endothermic heat generation due the DIR process cools the cell: its temperature becomes lower than 800 °C.

4. Discussion

4.1. Optimisation of the anode thickness for methane reforming

It has been shown in Section 3.1 that the rate of methane conversion into hydrogen increases with the anode thickness up to reach an asymptotic value. This effect has been explained by the limitation of the reforming reaction rates due to the dilution of the reactants with the products. Indeed, insufficient diffusion of the species through the anode hinders any efficient homogenisation. Consequently, only a small part of the anode is working regarding to the reforming process. Then, as the conversion zone is limited in the anode, the CH_4 conversion rate should decrease with increasing the fuel flow rate introduced at the cell inlet. This remark is illustrated in Fig. 20: the methane conversion determined at the OCV has been plotted as a function of the anode thickness for fuel flow rates varying from $\dot{n}^{\text{inlet}}_{CH_4} = 3.671 \times 10^{-5}$ mol s^{-1} to 29.372×10^{-5} mol s^{-1} (with S/C = 1, electrolyte thickness = 150 μm and active cell area = 98.5 cm^2). As expected, the methane conversion is found to be improved when the fuel flow rate is lowered. It is worth noting that the fuel utilisation (calculated for the standard ∼0.7 V cell polarisation in Fig. 21) follows the same trend than the methane conversion rate.

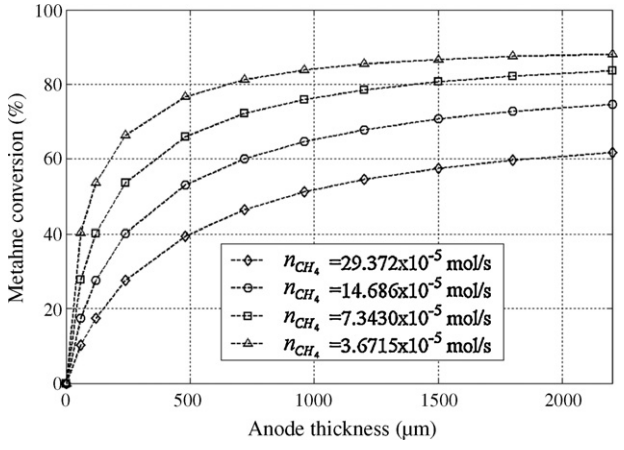

Fig. 20. Methane conversion calculated for different inlet methane flow rates and plotted as a function of the anode thickness (at OCV, $R = \dot{n}^{\text{inlet}}_{H_2O}/\dot{n}^{\text{inlet}}_{CH_4} = 1$, electrolyte thickness = 150 μm and active cell area = 98.5 cm^2).

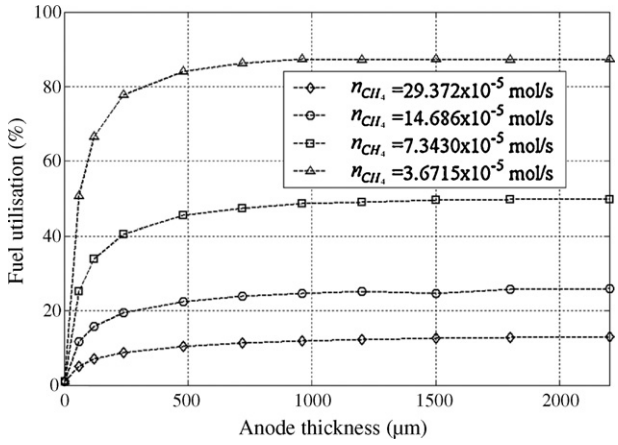

Fig. 21. Fuel utilisation calculated for different inlet methane flow rates and plotted as a function of the anode thickness (for $U_{\text{cell}} = 0.69$ V, $R = \dot{n}^{\text{inlet}}_{H_2O}/\dot{n}^{\text{inlet}}_{CH_4} = 1$, electrolyte thickness = 150 μm and active cell area = 98.5 cm^2).

From the methane conversion and fuel utilisation curves (Figs. 20 and 21), it can also be concluded that an anode thickness higher than 400–500 μm is required to reach sufficient CH_4 conversion and the highest achievable fuel utilisation.

Drescher et al. [25,26] have experimentally measured the methane conversion rate on a classical anodic cermet. In their test equipment, the wet methane mixture was flowing over both sides of a flat porous substrate (without electrolyte). The tests have been carried out at 915 °C, for a methane flux density of $\dot{N}_{CH_4} = 1.238 \times 10^{-4}$ mol cm^{-2} s^{-1} and a ratio $S/C = \dot{n}^{\text{inlet}}_{H_2O}/\dot{n}^{\text{inlet}}_{CH_4} = 3$. They have found that the methane conversion rate increases strongly up to an anode thickness of 600 μm. Beyond this value, the reactivity is observed to become less dependent of the anode thickness. The authors conclude from these results that, in their operating conditions, the depth of the reaction zone corresponds roughly to the half thickness of the anode substrate, *i.e.* ∼300 μm. To validate the present modelling tool on the basis of these results, simulations have been performed considering their operating conditions. However, the wet methane mixture has been assumed to flow on only one side of the cermet, the other side being covered by a dense electrolyte layer. The comparison with experimental points has been achieved assuming that these experimental values refer to the half thickness of the real anodic substrate. In Fig. 22, the comparison between the simulated curve and the experimental data from [25,26] is presented (with the experimental points expressed as a function of the half thickness of the real anodic substrate). A relatively good agreement is observed between the simulated curve and experimental data which allows validating partially the present model. The slight discrepancy observed can be attributed to the assumption done to take advantage of the experimental data. Furthermore, as mentioned by Lehnert et al. [9], the choice of the cermet microstructure parameters influences the methane conversion rate. For instance, they have demonstrated that the ratio ε/τ of porosity to tortuosity is the parameter that affects mostly the methane conversion. In their conditions, a 26.28% decrease in ε/τ compared to their standard cermet induces a 12.24% decrease in the methane conversion rate.

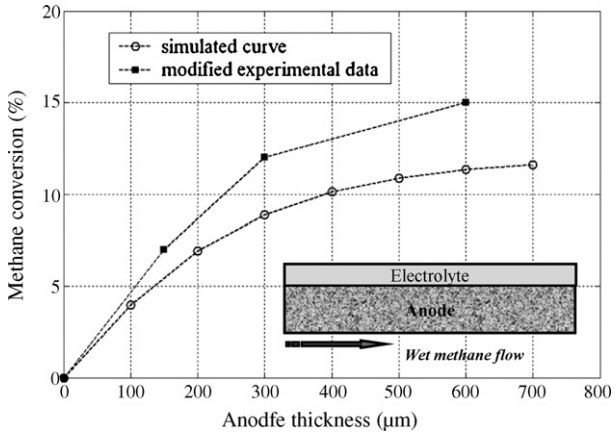

Fig. 22. Methane conversion plotted as a function of the anode thickness. The simulated curve has been obtained in the same conditions of temperature, molar flux density and steam to carbon ratio than the measured data from [25,26]. The experimental data have been modified to takes into account the methane flow condition (on one side only) (at OCV, $T = 915\,^{\circ}C$, $\dot{N}_{CH_4} = 1.238 \times 10^{-4}\,mol\,cm^{-2}\,s^{-1}$ and $R = \dot{n}^{inlet}_{H_2O}/\dot{n}^{inlet}_{CH_4} = 3$).

4.2. Electrical and thermal management of SOFC stack fed with methane in the boiler

For the considered SRU, autothermal conditions are found to be achieve for cell voltages ranging between ~680 mV and ~800 mV depending on the inlet fuel flow rates (Fig. 18). These conditions lead to a fuel utilisation decreasing from ~55% to ~40% with increasing the fuel flow rate (Fig. 17).

Regarding the studied application, *i.e.* a SOFC incorporated in a boiler, this autothermal mode of cell operation appears as a good compromise for the SOFC thermal management. Indeed, no thermal fluxes will flow between the stack and the insulating envelope. In addition, the cell thermal gradient is expected to be minimised since the endothermic heat absorption due to the reforming process will be exactly counter-balanced by the exothermic hydrogen oxidation heat release. This remark is illustrated in Fig. 23 where the cell temperature profile (Fig. 23a) and the associated thermal gradient (Fig. 23b) are plotted along the cell radius (for the third condition of gas feeding: see Table 3). The lowest thermal gradient along the cell is found to be achieved for a cell voltage higher than 700 mV but lower than 800 mV, corresponding to the calculated autothermal condition (Fig. 18).

The electrical efficiency ξ of the SRU is defined by the ratio of the electrical power generated by the SOFC over the amount of heat liberated by the complete combustion of fuel (the water produced by the combustion being assumed to remain as vapour)

$$\xi = \frac{U_{cell} I}{\dot{n}^{inlet}_{CH_4}\,NCV} \tag{18}$$

The net calorific value (NCV) of natural gas (=802.4 kJ mol^{-1} [27]) has been considered for the present study.

The efficiency map has been calculated for the considered SRU and is given in Fig. 24. Autothermal conditions, as determined in Fig. 18, lead to relatively poor electrical efficiencies. Indeed, the highest electrical efficiency, ranging around 45%,

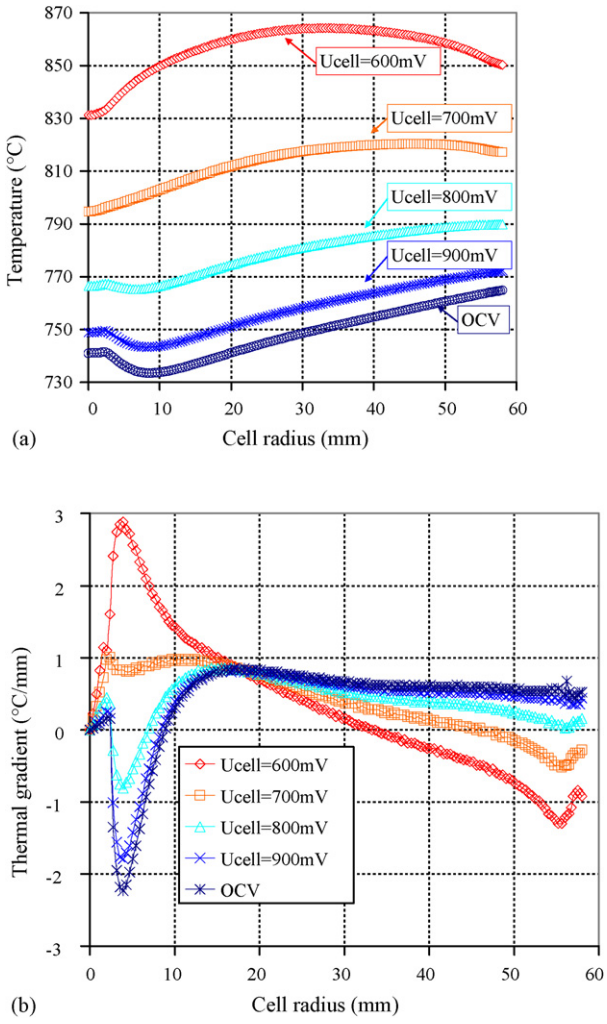

Fig. 23. Cell temperature profile and associated thermal gradient plotted as a function of the cell radius and for different cell polarisations (third condition of gas feeding: see Table 3). (a) Temperature taken at anode/electrolyte interface, (b) Thermal gradient dT/dr at anode/electrolyte interface.

is obtained with the lowest investigated methane flow rate (see Fig. 24). Consequently, higher cell polarisations (or lower methane flow rates) will be required to reach a more adequate efficiency regarding to the application. However, these last conditions are obtained with high fuel utilisations ($U_f > 60\%$) and induce high thermal gradients, both effects being potentially harmful for the cell durability.

In addition, the fuel dilution by nitrogen is found to lower the cell electrochemical performances by decreasing the OCV and simultaneously increasing the concentration overpotentials. Consequently, the dilution effect is expected to decrease further the electrical efficiency of SOFC operated directly with methane. Simulations have been performed with the same CH_4 flow rates as those given in Table 3. However, the total fuel flow rate has been kept constant to $29.372 \times 10^{-5}\,mol\,s^{-1}$ by adding nitrogen gas to the stream (with $R = \dot{n}^{inlet}_{H_2O}/\dot{n}^{inlet}_{CH_4} = 1$). The resulting electrical efficiencies (Fig. 25) are found to exhibit substantially lower performances than the ones without dilution (Fig. 24).

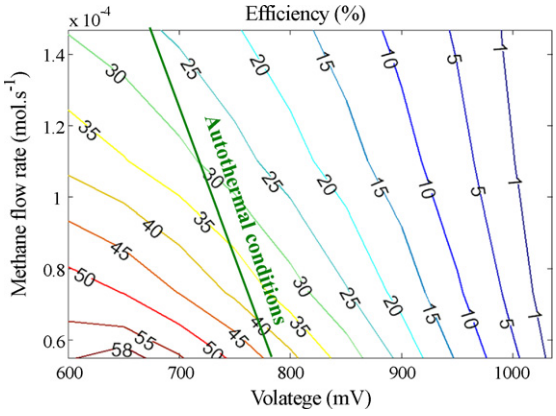

Fig. 24. Map of electrical efficiency plotted as a function of inlet methane flow rate and cell voltage (condition of gas feeding given in Table 3).

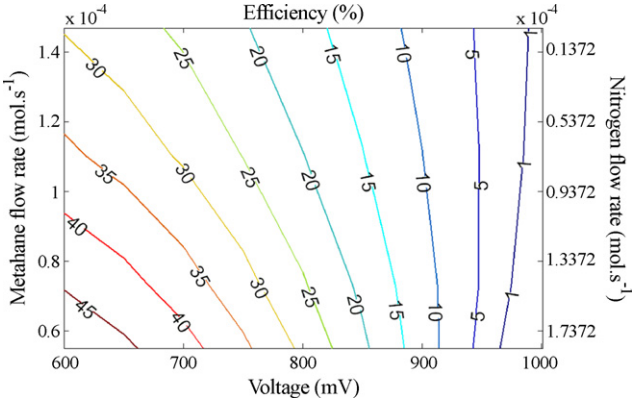

Fig. 25. Map of electrical efficiency plotted as a function of inlet CH_4 and N_2 flow rates and cell voltage (the total fuel flow rate has been kept constant to 29.372×10^{-5} mol s^{-1} by adding nitrogen gas to the stream with $R = \dot{n}^{\text{inlet}}_{H_2O}/\dot{n}^{\text{inlet}}_{CH_4} = 1$).

5. Conclusion

An in-house-model has been developed to study the thermal and electrochemical behaviour of a planar SOFC stack fed directly with methane and incorporated in a boiler. Simulations have been performed with Ni-YSZ cermet as the anodic material. It has been shown that the methane reforming into hydrogen is confined at the cell inlet in a limited anode volume. Therefore, a sufficient anode thickness is required to obtain the most efficient methane conversion. A sensitivity analysis, on both the anode thickness and the fuel flow rate, has allowed establishing that thicknesses higher than ~400–500 μm are required to achieve optimal electrochemical performances.

The DIR mechanisms and the impact of operating conditions on temperature gradients and electrical efficiencies have then been investigated considering anode supported cell geometry. It has been highlighted that the temperature gradient is minimised in the autothermal operating mode whereas, it appears to be significant at the cell inlet in exothermic or endothermic conditions. Thermal equilibrium in the stack has been found to be strongly dependent on radiative losses with the stack envelope. Electrochemical performance maps have been established as a function of methane flow rates and cell voltages. In the considered conditions, the best compromise regarding thermal equilibrium corresponds to the autothermal operating conditions leading to a fuel utilisation ranging between ~55% and ~40% and an electrical efficiency decreasing from ~45% to ~25%. Further simulations are in progress to determine the best compromise regarding electrochemical efficiency while maintaining thermal and mechanical satisfactory conditions.

Acknowledgments

The authors would like to thank Drs. S. Rosini and J. Mougin for many useful discussions and the critical reading of the manuscript. A part of this work has been obtained in the framework of a national research program called CIEL, led by S. Hody from Gaz de France and financed by the French National Research Agency ANR agency (contract number ANR-05-PanH-024).

References

[1] K. Ahmed, K. Foger, Catal. Today 63 (2000) 479–487.
[2] P. Vernoux, M. Guillodo, J. Fouletier, A. Hammou, Solid State Ionic 135 (2000) 425–431.
[3] S. Nagata, A. Momma, T. Kato, Y. Kasuga, J. Power Sources 101 (2001) 60–71.
[4] P.-W. Li, M.K. Chyu, J. Power Sources 124 (2003) 487–498.
[5] S. Campanari, P. Iora, J. Power Sources 132 (2004) 113–126.
[6] C. Stiller, B. Thorud, S. Seljebø, Ø. Mathisen, H. Karoliessen, O. Bolland, J. Power Sources 141 (2005) 227–240.
[7] D. Sánchez, R. Chacarteguei, A. Muñoz, T. Sánchez, J. Power Sources 160 (2006) 1074–1087.
[8] J.M. Klein, Y. Bultel, S. Georges, M. Pons, Chem. Eng. Sci. 62 (2007) 1636–1649.
[9] W. Lehnert, J. Meusinger, F. Thom, J. Power Sources 87 (2000) 57–63.
[10] T. Ackmann, L.G.J. de Haart, W. Lehnert, D. Stolten, J. Electrochem. Soc. 150 (6) (2003) A783–A789.
[11] P. Aguiar, C.S. Adjiman, N.P. Brandon, J. Power Sources 138 (2004) 120–136.
[12] B. Morel, J. Laurencin, Y. Bultel, F. Lefebvre-Joud, J. Electrochem. Soc. 152 (7) (2005) A1382–A1389.
[13] Y.-P. Chyou, T.-D. Chung, J.-S. Chen, R.-F. Shie, J. Power Sources 139 (2005) 126–140.
[14] D. Larrain, J. Van Herle, F. Maréchal, D. Favrat, J. Power Sources 118 (2003) 367–374.
[15] D. Larrain, J. Van Herle, F. Maréchal, D. Favrat, J. Power Sources 131 (2004) 304–312.
[16] K. Kendall, N.M. Minh, S.C. Singhal, in: S.C. Singhal, K. Kendall (Eds.), High Temperatures Solid Oxide Fuel Cells, Elsevier, Oxford, 2003, p. 200.
[17] K. Sasaki, M. Uchimura, K. Shiosaki, K. Susuki, K. Watanabe, H. Kusaba, Y. Teraoka, Proceedings of the Sixth European Solid Oxide Fuel Cell Forum, vol. 3, Lucerne, Switzerland, 2004, pp. 1534–1543.
[18] http://www-cast3m.cea.fr/cast3m/index.jsp.
[19] B. Todd, J.B. Young, J. Power Sources 110 (2002) 186–200.
[20] K. Girona, J. Laurencin, B. Morel, M. Petitjean, Y. Bultel, F. Lefebvre-Joud, Proceedings of the Seventh European Solid Oxide Fuel Cell Forum, Lucerne, Switzerland, 2006, File no. B113.
[21] J.W. Kim, A.V. Virkar, K.Z. Fung, K. Metha, S.C. Singhal, J. Electrochem. Soc. 146 (1) (1999) 69–78.
[22] O. Yamamoto, Electrochem. Acta 45 (2000) 2423–2435.

[23] D.L. Damn, A. Fedorov, J. Power Sources 143 (2005) 158–165.
[24] Science and technology of zirconia, In: A.H. Heuer and L.W. Hobbs (Eds.), Am. Ceramic Soc., vol. 5, pp. 655.
[25] I. Drescher, W. Lehnert, J. Meusinger, Electrochem. Acta 43 (1998) 3059–3068.
[26] W. Lehnert, J. Meusinger, E. Riensche, U. Stimming, Proceedings of the Second European Solid Oxide Fuel Cell Forum, vol. 1, Lucerne, Switzerland, 1996, pp. 143–152.
[27] Combustibles gazeux et principes de la combustion, Gaz de France Editors, Brochure B104 (1992).